ADVANCED FUNCTIONAL MATERIALS
www.afm-journal.de

Ultra-Sensitive Short-Wave Infrared Organic Photodetectors Enabled by a π-Conjugation Extended Proquinoid Electron Acceptor

Yeonsu Choi, Se Jeong Park, Seunghyun Oh, Un-Hak Lee, Seunghyun Rhee, Dong Ryeol Whang, Sein Chung, Juhyoung Jung, Kilwon Cho, Bo Ram Lee, Sung Cheol Yoon, Jae Won Shim, and Seo-Jin Ko**

Short-wavelength infrared (SWIR) light detection technologies have attracted considerable attention due to their broad applications in bioimaging, sensing, and optical communication. Despite this promise, achieving high-performance organic SWIR photodetectors (SWIR OPDs) remains a major challenge due to intrinsically weak photoresponse and sensitivity in this spectral region. Herein, a novel proquinoid-type non-fullerene acceptor (NFA), denoted as TQC-4Cl is reported, which exhibits an ultra-narrow band gap of 1.01 eV and a broad spectral response extending beyond 1200 nm, enabled via an aromatic-quinoid transformation strategy. Thermal annealing of the TQC-4Cl film significantly enhanced crystallinity and molecular ordering. Consequently, the optimized TQC-4Cl-based SWIR OPDs exhibit an exceptionally low dark current density (J_d) of 4.38×10^{-8} A cm^{-2}, noise current of 466 fA (at 4 Hz), and a high external quantum efficiency (EQE) of 13.66% at 1200 nm at −0.5 V bias, resulting in a shot-noise limited specific detectivity (D_{sh}*) of 1.06×10^{12} Jones and a noise current-based specific detectivity (D_n*) of 2.84×10^{11} Jones under the same bias conditions. The ideal phase-separated morphology and high crystallinity of the photoactive layer provide the beneficial condition enabling efficient charge extraction, suppressed bimolecular recombination, and reduced energetic disorder. Furthermore, the devices demonstrated long-term operational stability at 85 °C, underscoring their superior thermal durability. This study not only marks the advancement toward the realization of highly sensitive and thermally robust SWIR OPDs but also contributes to the rational molecular design strategies for ultra-narrow bandgap organic semiconductors for next-generation optoelectronic devices.

1. Introduction

The demand for short-wavelength infrared (SWIR, usually $\lambda = 1000$ to 3000 nm) light detection technology has risen owing to its wide range of applications such as health monitoring, remote sensing, bioimaging, optical communications, military fields, and night vision.[1] Traditionally, commercial SWIR photodetectors have relied on inorganic semiconductors such as germanium (Ge) and III-V compounds (InGaAs), which, while offering excellent performance, suffer from inherent limitations including high production cost, rigidity, and complex fabrication processes.[2] In contrast, organic photodetectors (OPDs) have emerged as a next-generation platform that combines mechanical flexibility, solution-processability, and spectral tunability, thereby enabling scalable fabrication of lightweight and wearable optoelectronic systems.[3] To date, considerable efforts to boost the device performances of OPDs have been made through the development of advanced device architectures, including photomultiplication-type designs.[4]

In addition to device-level advancements, a variety of molecular design strategies have been explored to innovate

---

U.-H. Lee, S.-J. Ko
Department of Energy Science and Engineering
Daegu Gyeongbuk Institute of Science and Technology (DGIST)
Daegu 42988, Republic of Korea
E-mail: sjko927@dgist.ac.kr

The ORCID identification number(s) for the author(s) of this article can be found under https://doi.org/10.1002/adfm.202517337

DOI: 10.1002/adfm.202517337

Y. Choi, S. J. Park, S. Rhee, J. Jung, S. C. Yoon
Photoenergy Research Center
Korea Research Institute of Chemical Technology (KRICT)
141 Gajeong-ro, Yuseong-gu, Daejeon 34114, Republic of Korea

S. J. Park, S. Rhee, B. R. Lee
School of Advanced Materials Science and Engineering
Sungkyunkwan University (SKKU)
Suwon 16419, Republic of Korea

S. Oh, J. W. Shim
School of Electrical Engineering
Korea University
Seoul 02841, Republic of Korea
E-mail: jwshim19@korea.ac.kr

photoactive materials, particularly narrow band-gap organic semiconducting materials (OSMs).[5] Among them, non-fullerene acceptors (NFAs) have been considered as a promising class of photosensitive materials, which exhibit suitable energy levels, high crystallinity, and low exciton binding energy.[6] Most NFAs are built upon donor–acceptor (D–A) conjugated frameworks, which enhance intramolecular charge transfer (ICT) and enable extended absorption into the near-infrared (NIR) region.[7] However, despite significant advances, extending the photoresponse of NFAs beyond 1000 nm to meet the stringent performance requirements of SWIR OPDs remains a critical challenge, primarily due to their intrinsic bandgap constraints and insufficient π-electron delocalization.[8]

To overcome this bottleneck and enable efficient photodetection beyond 1000 nm, quinoidal (Q)-based NFAs have recently attracted considerable attention as promising photoactive materials for SWIR OPDs.[9] Since the quinoid form is non-aromatic and energetically unstable compared to the aromatic form, it tends to recover the aromaticity by reorganizing the chemical bonding with adjacent moieties.[10] Likewise, the loss of aromaticity for neighboring rings is compensated by the reorganization of the recovered quinoidal unit.[11] Such successive quinoid-aromatic (Q-A) transformation facilitates the ideal π-electron delocalization over whole conjugated backbone, achieving the very reduced bond length alternation (BLA) with ultra-narrow band-gap and long-wavelength absorption behavior.[12] Therefore, the exploration of quinoid-type building blocks is a key strategy for the realization of SWIR OPDs.

In addition to the intrinsic quinoidal units, proquinoid-type molecules have been developed as a rational molecular design strategy to reduce their band gaps.[13] The “proquinoid” structure refers to a molecular system showing typical aromaticity but having the potential to undergo quinoid-like resonance form.[14] Since the aforementioned Q-A transformation to lower band gap is also effective for proquinoid-type molecules, they also exhibit the ultra-narrow band gap properties for the conjugated polymers[15] as well as small molecules.[16] Recently, proquinoid NFAs incorporating thieno[3,4-*c*]thiadiazole (TTD),[17] [1,2,3]triazolo[4,5-*f*]-2,1,3-benzothiadiazole (TBz),[18] and benzobisthiadiazole (BBT)[3b] have been developed as the state-of-the-art photoactive materials for SWIR OPDs and showed obvious sensitivity over 1000 nm wavelength. However, despite the photoresponsivity in the desired absorption range, it still suffers from the relatively low specific detectivity (D^*) due to low responsivity (R, < 0.1 A W^{-1}) and extremely high dark current density (J_{d}, > 10^{-6} A cm^{-2} at -0.5 V) at reverse bias.[3b,19]

Among the various proquinoid-type moieties, thiadiazolo quinoxaline (TQx) unit, which contains the electron-deficient thiadiazole and quinoxaline moieties, is also a good candidate for implementing SWIR absorption behavior.[20] The TQx moiety features an extended π-conjugation system and a deep lowest unoccupied molecular orbital (LUMO) energy level, enabling efficient charge transfer and exciton dissociation, which are key factors for achieving high photodetection performance.[21] Due to these desired optoelectronic properties, TQx unit has been adopted as a monomer in conjugated polymers for SWIR OPDs. Previous studies by Maes et al.[22] and Leem et al.[23] have demonstrated that OPDs incorporating TQx-based copolymers can achieve a high external quantum efficiency (EQE) of ≈20% in the SWIR range. However, these devices also displayed high dark current, resulting in inferior detectivity under reverse bias. Thus, the development of new materials that satisfy both high photoresponsivity and detectivity still remains a critical challenge for advancing SWIR OPD technology.

In this work, a proquinoid-type NFA, TQC-4Cl, was developed as a highly sensitive photoactive material as an electron acceptor with poly([2,6′-4,8-di(5-ethylhexylthienyl)benzo[1,2-b;3,3-b]dithiophene]{3-fluoro-2[(2-ethylhexyl)carbonyl]thieno-[3,4-b]thiophenediyl}) (PTB7-Th) as electron donor for SWIR OPDs (**Figure** 1a). Guided by a molecular design strategy aimed at reducing the band gap, TQC-4Cl shows an ultra-narrow optical band gap (E_g^{opt} = 1.01 eV) with an extended light absorption edge reaching up to a wavelength of 1233 nm. DFT calculations reveal that the frontier molecular orbitals (FMOs) exhibit well-delocalized π-electron densities in both the LUMO and the highest occupied molecular orbital (HOMO), which facilitate efficient charge transport and enhanced oscillator strength. The SWIR OPDs based on PTB7-Th:TQC-4Cl exhibited clear photoresponse beyond 1200 nm, along with an exceptionally low J_{d} below 10^{-7} A cm^{-2} at −0.5 V. Thermal annealing of the devices improved molecular crystallinity and intermolecular packing, leading to a red-shift in the EQE spectrum and an enhanced external quantum efficiency of up to 13.7% at 1200 nm. As a result, the optimized TQC-4Cl-based organic photodetectors (OPDs), exhibiting high EQE and effectively suppressed J_{d}, achieved a R of 0.132 A W^{-1} and a noise current of 466 fA (at 4 Hz), yielding a shot noise-limited specific detectivity (D_{sh}*) of 1.06 × 10^{12} Jones and noise current-based D^* (D_n*) of 2.84 ×10^{11} Jones at 1200 nm wavelength under −0.5 V bias. These metrics represent one of the highest values reported to date among SWIR OPDs. The devices also showed excellent response speed, broad linear dynamic range (LDR) up to 77.2 dB. Moreover, since exposure to high temperatures could lead to material degradation and device performance deterioration, high thermal stability of photoactive materials is crucial for reliable and long-term operation.[24] The TQC-4Cl-based OPDs maintained stable performance for over 1800 h under continuous thermal exposure at 85 °C, confirming their excellent thermal durability. This work highlights the potential of proquinoid-type organic semiconductors as promising candidates for highly sensitive and thermally stable SWIR OPDs.

2. Results and Discussion

2.1. Molecular Design, Synthesis, and Optoelectronic Characteristics

An A-D-Q-D-A type NFA, TQC-4Cl, was synthesized as the following design strategies to ensure SWIR light absorption behaviors: 1) the proquinoidal TQx unit as the central core of the

---

D. R. Whang
Department of Advanced Materials
Hannam University
Daejeon 34054, Republic of Korea

S. Chung, K. Cho
Department of Chemical Engineering
Pohang University of Science and Technology
Pohang 37673, Republic of Korea

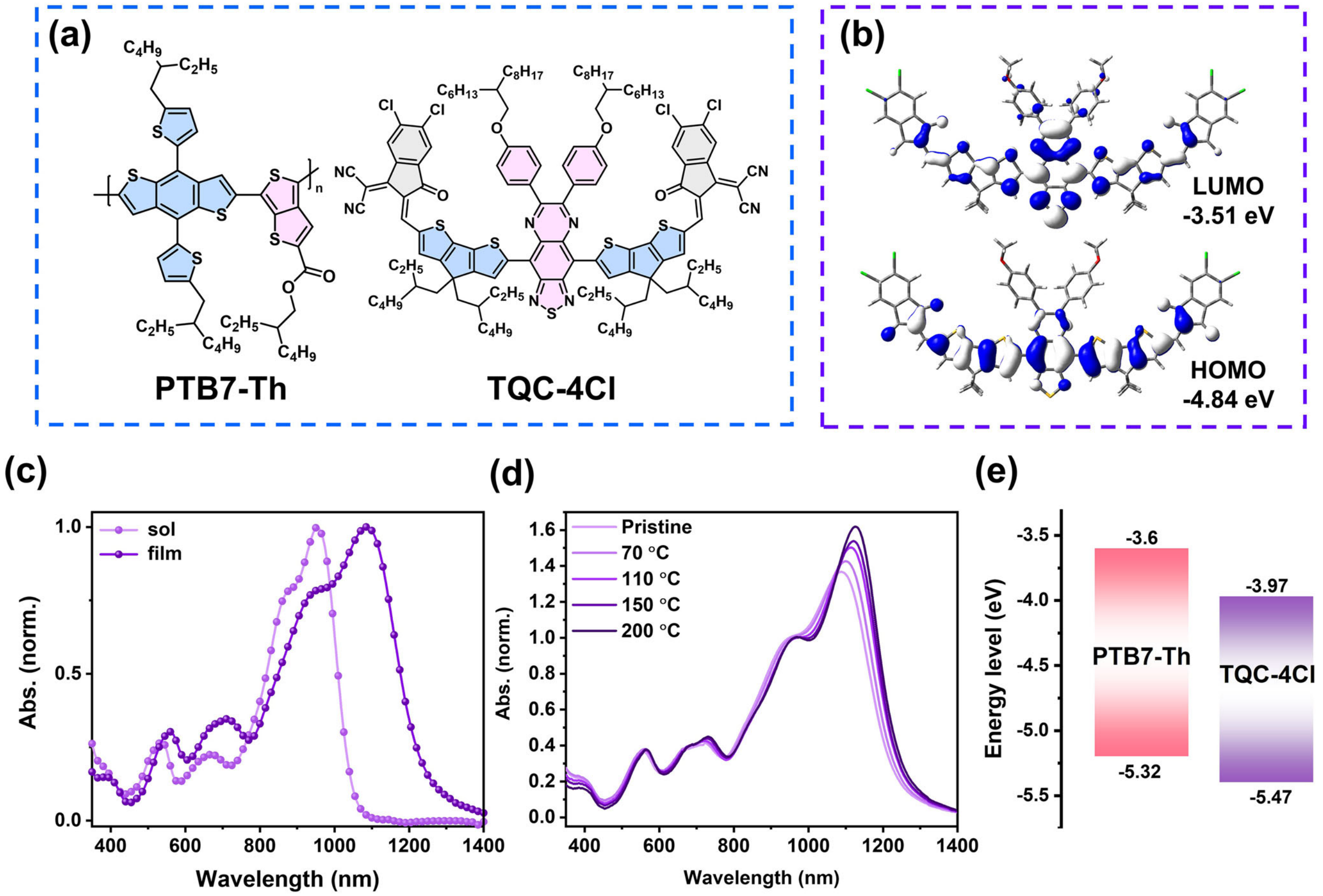

Figure 1. a) Chemical structure of electron donor PTB7-Th and acceptor TQC-4Cl. b) calculated HOMO/LUMO electron distribution of TQC-4Cl. c) Normalized absorption spectra of TQC-4Cl for chloroform solution and as-casted thin film. d) Temperature-dependent absorption spectra of TQC-4Cl films. e) Energy level diagram of PTB7-Th and TQC-4Cl.

target molecule, which induces efficient electron delocalization over the whole conjugated backbone; 2) the CPDT unit as a π-bridge exhibiting low resonance stabilization energy as well as the strong electron-donating property to enhance intramolecular charge transfer (ICT) effect; 3) a strong electron-withdrawing end group to facilitate the aromatic-quinoid transformation in the main backbone and to enable molecular planarity. The synthetic route of TQC-4Cl is shown in **Scheme 1**. The brominated proqunoidal TQx was coupled with compound 1 by Stille coupling reaction to afford a compound 2 with a yield of 77%. Then compound 2 was formylated by Vilsmeier-Haack reaction with dimethyl formamide (DMF) and phosphorous oxychloride ($POCl_3$) to give compound 3, with a yield of 85%. Then, the target molecule TQC-4Cl was obtained via the Knoevenagel condensation from compound 3 and 2-(5,6-dichloro-3-oxo-2,3-dihydro-1H-inden-1-ylidene)-malononitrile (IC-2Cl) with a yield of 67%. The chemical structures of the final product and intermediates were characterized by ^{1}H and ^{13}C nuclear magnetic resonance (NMR) spectroscopy, revealing that all compounds were successfully isolated (Figures S2–S8, Supporting Information). TQC-4Cl showed high solubility in common organic solvents, such as dichloromethane, chloroform, trichloroethylene, and toluene, thereby providing versatility in the choice of solvents for solution-based processing. The thermal property of TQC-4Cl was evaluated by thermogravimetric analysis (TGA), where decomposition temperatures (T_d) of 346 °C with 5% weight loss were observed (Figure S9, Supporting Information). Additionally, no thermal transition of TQC-4Cl is observed between 25 and 280 °C in the differential scanning calorimeter (DSC) curve, suggesting excellent thermal robustness. The thermal stability of TQC-4Cl facilitates the fabrication of thermally stable OPDs in terms of both processability and long-term thermal tolerance.[25]

Density functional theory (DFT) calculation was performed on the B3LYP/6-31G** basis set in order to investigate the electronic structure of TQC-4Cl. For computational simplicity, the alkyl chains were replaced by methyl chains. Figures 1b and S10a (Supporting Information) display frontier molecular orbitals (FMOs) and the optimized geometry of TQC-4Cl, respectively. The electron clouds of FMOs, HOMO, and LUMO are well-distributed over the entire conjugated backbone and well-overlapped with each other. In addition, the optimized molecular structure exhibits a highly planar molecular geometry with very small dihedral angles between aryl rings approaching zero degrees owing to the stabilized electron delocalization by quinoid-aromatic transformation as well as the intramolecular electrostatic interactions such as S—N and N—H non-covalent bonding.

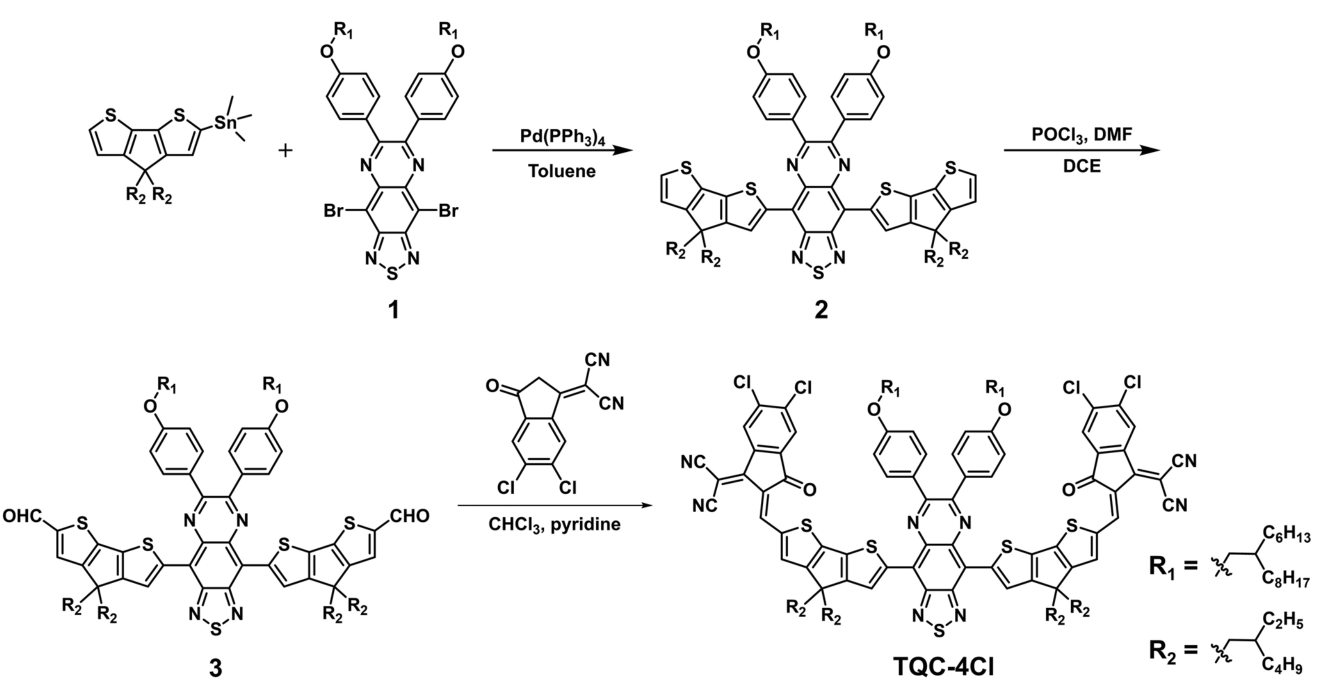

Scheme 1. Synthetic routes for TQC-4Cl.

The simulated absorption spectra of TQC-4Cl in the chloroform solvation model were obtained using time-dependent (TD)-DFT calculations (Figure S11, Supporting Information). According to the simulated absorption spectra, the most intense absorption band at 1086 nm indicated the HOMO → LUMO transition peak, while the second and third bands at 636 and 565 nm were ascribed to the HOMO → LUMO + 4 and HOMO – 2 → LUMO peaks, respectively. The intensity of oscillator strength, which is proportional to the square of the transition dipole moment, is generally determined by the electron cloud overlapping between the lower state and upper state.[26] It is consistent with the predicted electron distribution results, where both electron clouds of HOMO (lower state) and those of LUMO (upper state) are well-delocalized and overlapped each other as mentioned above. As a result, the electronic structure of TQC-4Cl is suitable for achieving high molar absorptivity, facilitating high photoresponsivity in SWIR region.

The experimental ultraviolet-visible (UV-vis) light absorption spectra of TQC-4Cl in chloroform solution and as casted thin film are recorded (Figure 1c), and the related parameters are summarized in **Table 1**. In diluted chloroform solution, TQC-4Cl exhibits an obvious 0-0 absorption peak at 954 nm as the maximum absorption wavelength (λ_{max}), which suggests the strong pre-aggregation states of TQC-4Cl in solution. In the film state, TQC-4Cl shows a broad light absorption range from visible to SWIR region owing to its distinct chemical structure, such as highly planarity and favorable quinoid-aromatic transformation, leading to effective electron delocalization along the conjugated backbone. Compared with the solution state, TQC-4Cl shows significantly red-shifted spectra with λ_{max} of 1086 nm. The onset of absorption wavelength (λ_{onset}) for TQC-4Cl was observed as 1233 nm, the corresponding optical band gap (E_g^{opt}) was calculated as 1.01 eV, which is one of the narrowest E_g^{opt} for NFAs covering the SWIR range. In addition, the temperature-dependent absorption spectra of TQC-4Cl thin film were collected in the range of pristine to 200 °C, revealing that the λ_{max} of TQC-4Cl film is sequentially red-shifted along with the increase of vibronic peaks from 1086 to 1126 nm as the annealing temperature increased (Figure 1d). It could be attributed to the planar structure of TQC-4Cl beneficial for intermolecular packing and enhanced crystallinity by thermal treatment. In order to obtain further insight into the structural evolution, 2D grazing incidence wide-angle X-ray scattering (GIWAXS) measurements were conducted. The GIWAXS patterns revealed that TQC-4Cl films exhibited face-on dominated bimodal molecular packing structures. Notably, the crystallinity of TQC-4Cl films increased as the annealing

Table 1. Optical and electrochemical properties of TQC-4Cl.

	$\lambda_{\text{max,abs}}$ [nm][a] Solution	$\lambda_{\text{max,abs}}$ [nm] Film	λ_{edge} [nm] Film	E_g^{opt} [eV][b]	E_{HOMO} [eV][c]	E_{LUMO} [eV][d]	E_g^{CV} [eV][e]
TQC-4Cl	953	1086	1233	1.01	−5.47	−3.97	1.50

[a] From diluted chloroform solution; [b] $E_g^{opt} = 1242 / \lambda_{\text{onset}}$ eV; [c] $E_{HOMO} = -(E_{ox}^{onset} - \mathrm{E}_{1/2}(\text{ferrocene}) + 4.8)$ eV; [d] $E_{LUMO} = -(E_{red}^{onset} - \mathrm{E}_{1/2}(\text{ferrocene}) + 4.8)$ eV; [e] $E_g^{CV} = E_{LUMO} - E_{HOMO}$.

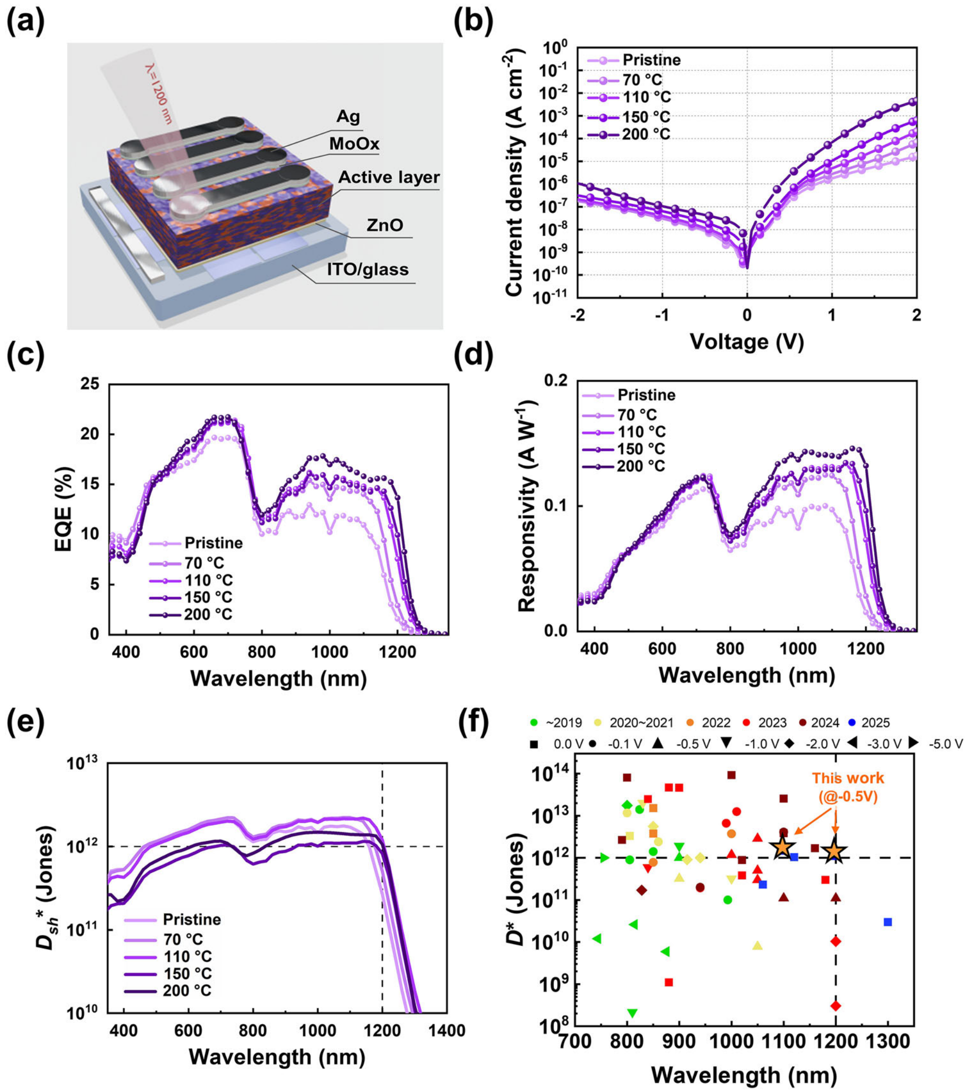

Figure 2. a) OPD device architecture, b) *J-V* characteristics under dark conditions, c) EQE spectra under AM 1.5G illumination at 100 mW cm^{-2}, and d) corresponding responsivity spectra of the OPDs fabricated under varying annealing temperature. e) Calculated D_{sh}* of the OPDs under shot-noise-limited conditions. Shot-noise was obtained at $V = -0.5$ V. f) Comparison of D_{sh}* attained at various incident wavelengths of previously reported OPDs.

temperature increased (Figure S13, Supporting Information). Although the d-spacing, such as lamellar and π-π stacking distances, remained largely unchanged by thermal annealing up to 200 °C, the crystal coherence length (CCL) of TQC-4Cl is significantly increased in both the in-plane (IP) (100) (from 72.5 to 202.0 Å) and out-of-plane (OOP) (010) (from 22.1 to 46.0 Å) directions. These results are in good agreement with the temperature-dependent absorption spectra, suggesting that the thermal treatment could be an effective strategy to enhance the molecular ordering and charge transport properties of TQC-4Cl films.

The frontier energy levels of TQC-4Cl were determined by cyclic voltammetry (Figure S14, Supporting Information). The oxidation and reduction potentials of TQC-4Cl film revealed HOMO and LUMO energy levels of −5.47 and −3.97 eV, respectively. They are suitable for energetic alignment with PTB7-Th which HOMO and LUMO energy levels were obtained as -5.32 and -3.60 eV, respectively (Figure 1e). The significant energy barrier between donor and acceptor possibly forms a favorable energy gradient and effectively suppresses the leakage current in OPD devices.

2.2. Device Fabrication and OPD Characteristics

To assess the photodetection properties of TQC-4Cl, OPD devices were fabricated in the structure of ITO/ZnO/PTB7-Th:TQC-4Cl/MoO$_x$/Ag (**Figure 2a**). To optimize the device performance, composition ratio, and solution concentration of PTB7-Th:TQC-4Cl were systematically investigated, and the corresponding results are provided in (Figures S15–S17, Supporting Information). The photoactive layer was annealed at 70, 110, 150, and 200 °C to examine the effect of thermal treatment on SWIR device performance. The resulting parameters of OPDs with PTB7-Th:TQC-4Cl blend are shown in Figure 2b–e, and the corresponding

Table 2. Device performance of OPDs based on PTB7-Th:TQC-4Cl with different annealing temperatures at −0.5 V bias voltage.

Ann. Temp. [°C]	J_d [A cm^{-2}]	EQE [%]$^{a)}$	EQE [%]$^{b)}$	R [A W^{-1}]$^{a)}$	R [A W^{-1}]$^{b)}$	D_{sh}* [Jones]$^{a)}$	D_{sh}* [Jones]$^{b)}$
Pristine	8.53×10^{-9}	10.93	1.58	0.097	0.015	1.71×10^{12}	2.69×10^{11}
70	9.81×10^{-9}	14.01	2.92	0.124	0.028	2.22×10^{12}	5.04×10^{11}
110	1.17×10^{-8}	14.79	7.54	0.131	0.073	2.11×10^{12}	1.19×10^{12}
150	2.07×10^{-8}	14.55	9.94	0.129	0.096	1.10×10^{12}	8.20×10^{11}
200	4.38×10^{-8}	15.80	13.66	0.140	0.132	1.40×10^{12}	1.06×10^{12}

$^{a)}$ Measured at 1100 nm wavelength; $^{b)}$ Measured at 1200 nm wavelength.

values at 1100 and 1200 nm wavelength are summarized in **Table 2**.

The dark current density (J_d) characteristics of the PTB7-Th:TQC-4Cl based devices were evaluated by sweeping the voltage from −2 to 2 V, as shown in Figure 2b. At a reverse bias of −0.5 V, J_d gradually increased with rising annealing temperature, which can be attributed to the enhanced transport of thermally activated carriers within the photoactive layer. The pristine device exhibited 8.53×10^{-9} A cm^{-2}, while the 200 °C annealed device showed a 4.38×10^{-8} A cm^{-2}. Although the J_d of the 200 °C annealed device is higher, it still remains at a relatively low level, maintaining a favorable dark current for the SWIR photodetector. Under forward bias conditions, J_d values increased with annealing temperature, reflecting enhanced charge transport characteristics influenced by improved molecular ordering and reduced charge recombination losses, rather than a direct increase in effective mobility.[27]

To quantitatively assess the influence of thermal annealing on the SWIR photo response, the EQE and R spectra of the SWIR OPDs based on PTB7-Th:TQC-4Cl are examined in Figure 2c,d, respectively. The R is defined by the following equation:

$$R = \frac{EQE}{100\%} \times \frac{\lambda}{1240\ (\text{nm W A}^{-1})} \tag{1}$$

where λ is the incident wavelength, any variation in EQE is reflected proportionally in R. As the annealing temperature increases, both the EQE and R spectra exhibit a gradual red-shift and enhanced magnitude throughout the NIR–SWIR region (800–1200 nm), as shown in Figure 2c,d. "At 1100 nm, EQE remained above 10% throughout the entire annealing temperature series, increasing steadily from 10.93% in the pristine device to 15.80% after annealing at 200 °C. At 1200 nm, the EQE showed a notable enhancement, rising from 1.58% in the pristine device to 2.92%, 7.54%, 9.94%, and 13.66% for devices annealed at 70, 110, 150, and 200 °C, respectively. As the R is directly proportional to EQE, it exhibited a similar temperature-dependent trend. At 1100 nm, R increased from 0.097 A W^{-1} (pristine) to 0.140 A W^{-1} after annealing at 200 °C. At 1200 nm, R improved significantly from 0.015 A W^{-1} in the pristine device to 0.028, 0.073, 0.096, and 0.132 A W^{-1} for devices treated at 70, 110, 150, and 200 °C, respectively. This pronounced enhancement in R constitutes a critical figure of merit for high-performance OPDs, as it directly correlates with device sensitivity. In particular, the markedly improved R at 1200 nm highlights the strong potential of these devices for short-wave infrared (SWIR) photodetection, where efficient photon harvesting in this spectral region is essential. However, further increasing the annealing temperature beyond a threshold (e.g., 250 °C) led to degradation in the optoelectronic properties (Figure S18 and Table S6, Supporting Information).

The shot noise-limited specific detectivity, D_{sh}* of the SWIR OPDs with PTB7-Th:TQC-4Cl blend was calculated from the R and J_d using

$$D_{sh}{}^{*} = \frac{R}{\sqrt{2qJ_d}} \tag{2}$$

where q is the elementary charge (1.602×10^{-19} C). As shown in Figure 2e, all devices exhibited D_{sh}* exceeding 10^{12} Jones at 1100 nm, registering values of 1.71×10^{12}, 2.22×10^{12}, 2.11×10^{12}, 1.10×10^{12}, and 1.40×10^{12} Jones for the pristine, 70, 110, 150, and 200 °C annealed OPDs, respectively. At 1200 nm, the device annealed at 200 °C achieved 1.06×10^{12} Jones at −0.5 V reverse bias, remaining within the 10^{2} Jones regime. Although the 200 °C-annealed PTB7-Th:TQC-4Cl based device exhibited a slight increase in J_d, the concurrent enhancement in R enabled it to exceed the 10^{12} Jones level at 1200 nm. The D_{sh}* value of the PTB7-Th:TQC-4Cl based device surpasses those previously reported values for SWIR OPDs, as summarized in Figure 2f. To evaluate the device reproducibility, D_{sh}* values at 1200 nm were determined from the J_d measurements of ten independently fabricated devices under each annealing condition; the corresponding averages and standard deviations are presented in Figure S19 (Supporting Information). Furthermore, the device annealed at 200 °C, which exhibited the highest EQE across the SWIR region, maintained excellent electrical stability during reverse bias sweeps from −0.5 to −5 V. Notably, the EQE at 1200 nm increased progressively with increasing applied bias, from 15.18% to 17.32%, 20.23%, 22.10% and finally reached 25.13% at −5 V (Figure S20, Supporting Information) — a remarked high value, thereby demonstrating the device's superior operational robustness under practical operating conditions.

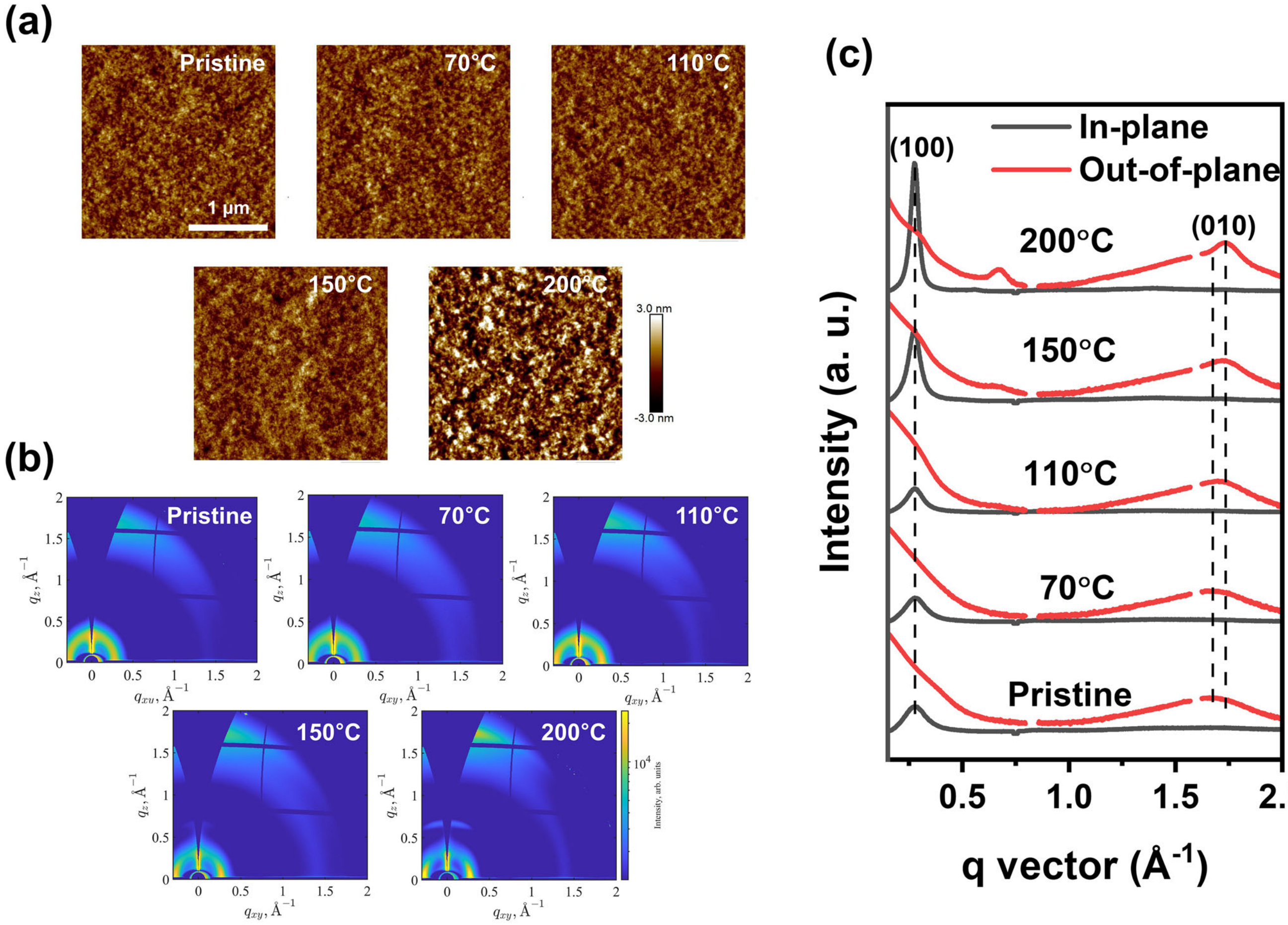

Figure 3. a) AFM height images, b) 2D GIWAXS images, and c) corresponding line-cut profiles of PTB7-Th:TQC-4Cl blended films with different annealing temperatures; pristine, 70, 110, 150, and 200 °C.

2.3. Morphological and Crystallinity Characteristics

To investigate the film morphology of photoactive layers, atomic force microscopy (AFM) measurements were performed, and the corresponding height images are shown in **Figure** 3a. The PTB7-Th:TQC-4Cl blend films exhibited uniform and smooth surfaces without excessive aggregation, which is favorable for efficient charge transport. The root-mean-square roughness values were measured to be 0.637, 0.634, 0.653, 0.657, and 1.280 nm for the pristine and 70, 110, 150, and 200 °C annealed PTB7-Th:TQC-4Cl films, respectively. While the films annealed up to 150 °C exhibited no significant change in surface morphology, the film annealed at 200 °C showed a pronounced increase in surface roughness. This increase is likely attributed to enhanced molecular crystallinity and the formation of a larger phase-separated domain.

To acquire further understanding of film morphology, 2D-GIWAXS measurement was performed. Figure 3b shows the diffraction pattern images of PTB7-Th:TQC-4Cl blend films with different annealing temperatures: pristine, 70, 110, 150, and 200 °C. The corresponding IP and OOP line profiles are provided in Figure 3c. The detailed crystallographic parameters were summarized in Table S7 (Supporting Information). The GIWAXS patterns revealed that all PTB7-Th:TQC-4Cl blend films displayed face-on orientation with clear lamellar stacking (100) peaks in the IP direction located at 0.27 Å^{-1} and π-π stacking (010) peaks in the OOP direction located at 1.67 (pristine, 70 °C), 1.73 (110, 150 °C), and 1.74 (200 °C) Å^{-1}, respectively. Comparison with the TQC-4Cl neat film shows that the crystalline structure of the PTB7-Th:TQC-4Cl blend film is mainly attributed to TQC-4Cl, with its (100) in the IP and (010) in the OOP diffraction peaks positioned at 0.28 and 1.73 Å^{-1}, respectively. Moreover, thermal annealing led to enhanced film crystallinity, as evidenced by the gradually reduced π-π stacking distances from 3.76 Å (pristine, 70 °C) to 3.63 Å (110, 150 °C) and further to 3.61 Å (200 °C). The CCL for the (100) diffraction in the IP direction also increased with thermal annealing, calculated to be 60.8, 63.5, 74.4, 95.9, and 128.5 Å for pristine, 70, 110, 150, and 200 °C PTB7-Th:TQC-4Cl films, respectively. While the CCL of blend films for the (010) diffraction in the OOP direction remained similar at lower annealing temperatures (13.5, 13.3, and 12.8 Å for pristine, 70, 110 °C), significantly larger values of 35.1 and 52.8 Å were observed at 150 and 200 °C. These results indicate that the thermal annealing process of photoactive layers promotes closer molecular packing and larger crystalline domains, thereby improving charge transport pathways, which contribute to enhanced charge

Table 3. Charge-carrier dynamics and energetic disorder parameters for PTB7-Th:TQC-4Cl OPD devices.

Ann. Temp. [°C]	t_{ex} [µs]	t_{re} [ms]	E_u [meV]
Pristine	0.96	2.39	19.56
70	0.79	2.61	19.30
110	0.75	2.82	18.65
150	0.69	3.07	17.60
200	0.33	4.98	17.12

extraction (albeit with slightly increased J_d) and higher EQE. Electrochemical impedance spectroscopy (EIS) measurements were additionally performed under open-circuit conditions to confirm the reduction of in-bulk deep-traps associated with enhanced crystalline properties (Figure S23, Supporting Information). The recombination resistance of the devices increased markedly from 1.36 kΩ in the pristine device to 7.37 kΩ in the 200 °C-annealed device, further supporting suppressed charge recombination and improved charge transport.

2.4. Carrier Dynamics and Energetic Disorder

We investigated the charge carrier dynamics and energetic disorder in PTB7-Th:TQC-4Cl-based OPDs to elucidate the underlying mechanism behind the gradual enhancement of EQE depending on the thermal annealing. The relevant data are summarized in **Table 3**. Transient photocurrent (TPC) and transient photovoltage (TPV) measurements are presented in **Figure 4**a,b, respectively. As shown in Figure 4a, the charge extraction time (t_{ex}) progressively decreased as the annealing temperature increased from the pristine state to 200 °C. Specifically, t_{ex} was reduced from 0.96 µs in the pristine device with increasing annealing temperature, and exhibited a marked drop to 0.33 µs in the device annealed at 200 °C. This abrupt reduction indicates a significant improvement in carrier transport, likely due to the formation of ideal percolation pathways facilitating efficient charge carrier transport. A similar trend was observed in the TPV measurements (Figure 4b), where the recombination time (t_{re}) progressively increased from 2.39 ms as the annealing temperature rose, with a substantial increase to 4.98 ms at 200 °C. These results indicate that thermal annealing suppresses bimolecular recombination and facilitates more balanced charge transport, particularly at elevated annealing temperatures. According to the changes of film morphology revealed by AFM and GIWAXS measurements, the structural evolution driven by thermal annealing provided the more efficient charge transport pathways as well as the suppressed charge recombination sites with fewer trap-rich interfaces.[28] Complementary photo-charge extraction by linearly increasing voltage (CELIV) measurements (Figure S25, Supporting Information) corroborated that the intrinsic drift mobility is effectively unchanged across the annealing series. The effective mobility (μ_{eff}) varied only within 2.3-3.6 × 10^{-4} $\mathrm{cm^2\ V^{-1}s^{-1}}$, from the pristine film to the device annealed at 200 °C. Such marginal variation indicates that the thermal treatment does not

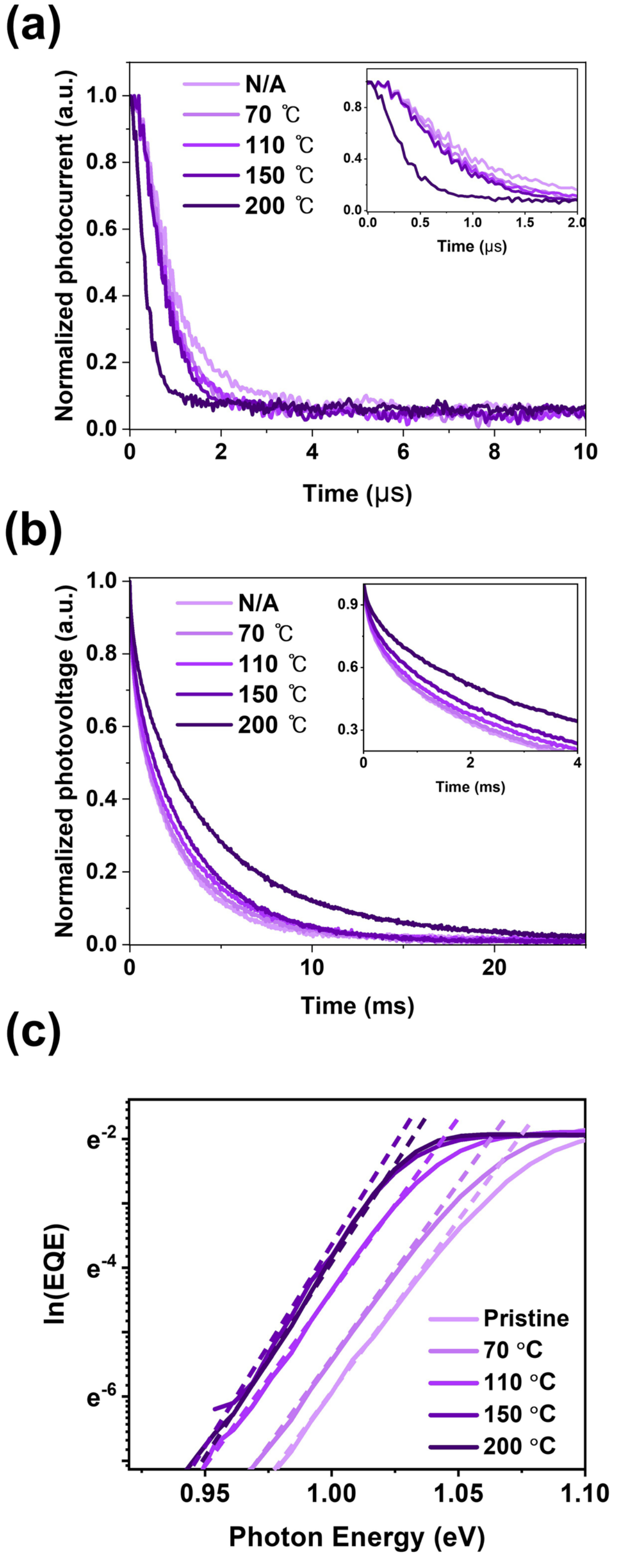

Figure 4. a) Transient photocurrent (TPC) and b) transient photovoltage (TPV) decay kinetics of TQC-4Cl-based OPDs with different annealing temperatures. c) Urbach energy extracted from EQE spectra.

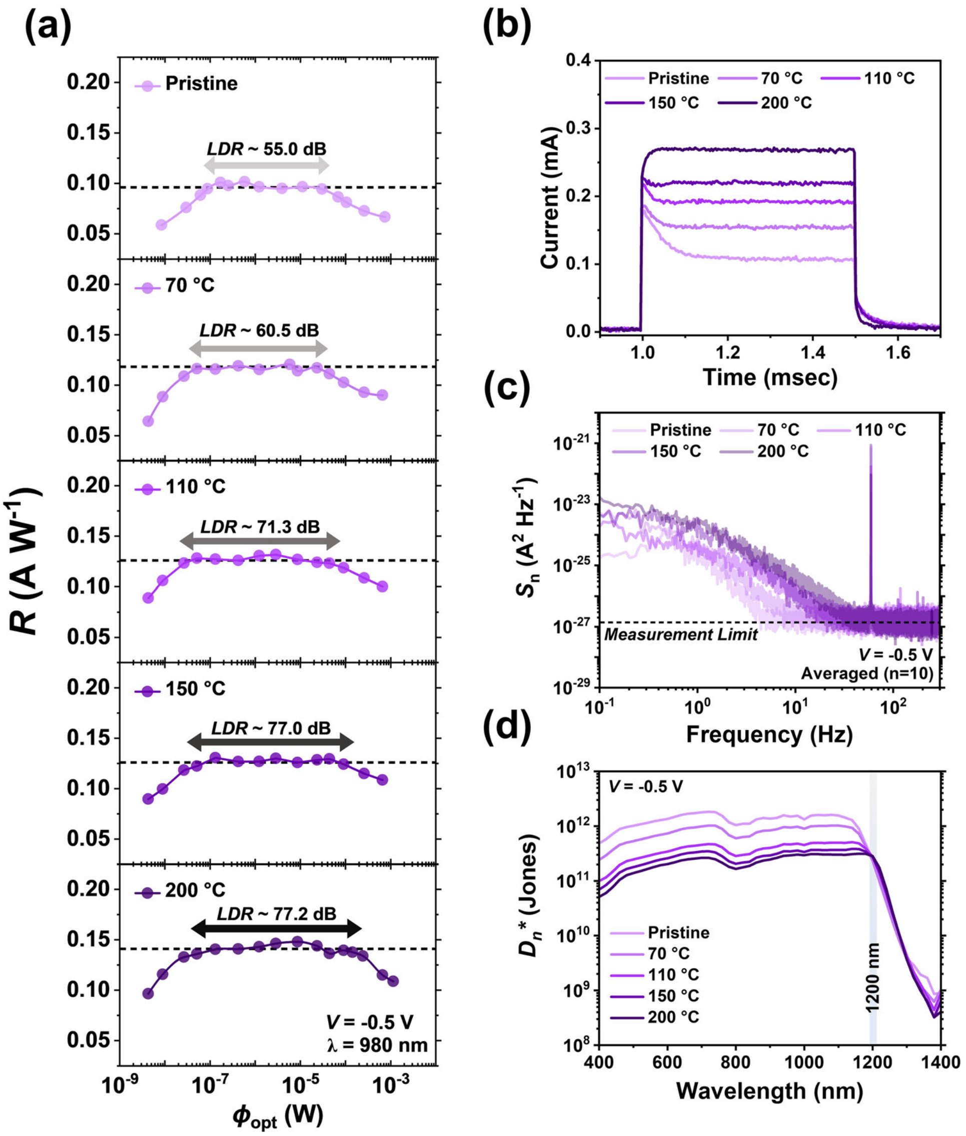

Figure 5. a) Linear dynamic range (LDR) of TQC-4Cl-based OPD devices with different annealing temperatures under $\lambda = 980$ nm illumination of varying optical power at −0.5 V bias. b) Rise-fall response time measurements of the devices. c) Spectral noise density of the devices. d) Extrapolated D_n* spectra.

create fundamentally faster transport channels; instead, the pronounced improvements in t_{ex} and t_{re} arise from a reduced trap population and suppressed bimolecular recombination, revealed by TPV measurements.

The improvements in film morphology and molecular ordering are closely associated with a reduction in energetic disorder as well as the favorable charge extraction and suppressed bimolecular recombination, as evidenced by the Urbach energy (E_u) extracted from the EQE spectra (Figure 4c). The E_u, which quantifies the steepness of the exponential absorption tail near the band edge, reflects the density of localized states induced by structural disorder. It was calculated using the following relationship:

$$ln\left(EQE\right) = c + \frac{h\nu}{E_u} \tag{3}$$

where c is a constant and $h\nu$ is the photon energy.[29] The calculated E_u decreases from 19.56 to 17.12 meV with increasing annealing temperature. This reduction in energetic disorder suggests a lower density of trap states within the active layer, which in turn contributes to enhanced charge carrier mobility. This noticeable improvement can be explained by the crystallinity and surface morphology of the active layer.

2.5. Linearity, Response Speed, and Noise Performance

Figure 5a presents the photocurrent measurements of the devices upon $\lambda = 980$ nm laser illumination at varying optical power (Φ_{opt}). Φ_{opt} calibration using a neutral-density filter enabled the precise realization of the linear dynamic range (LDR) of each device. The SWIR-optimum device exhibited the broadest

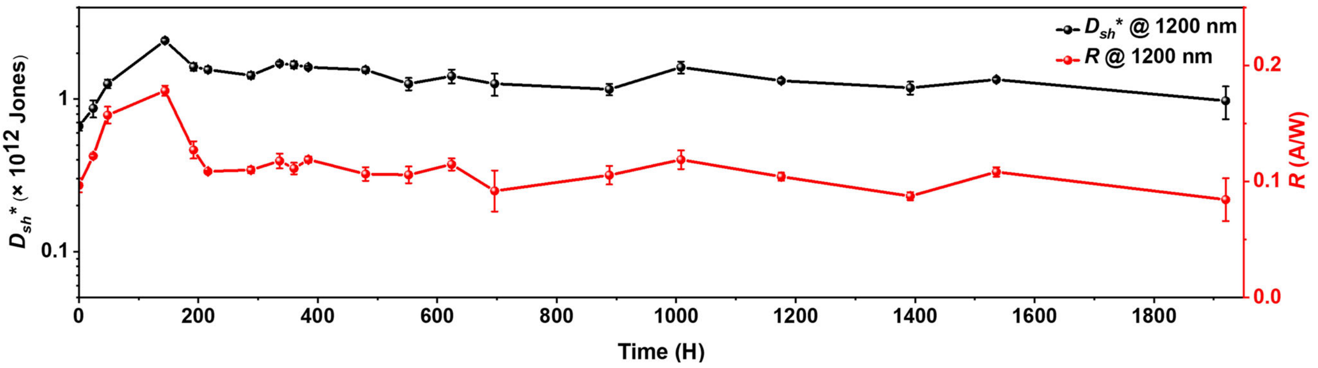

Figure 6. Long-term stability test of SWIR OPDs based on PTB7-Th:TQC-4Cl (fabricated with thermal annealing at 200 °C). The devices were continuously aged at 85 °C conditions. ($n = 4$).

LDR of 77.2 dB, in which the extension occurred primarily at high Φ_{opt}. This behavior is ascribed to annealing-induced reductions in deep tail states and energetic disorder in the photoactive layer, corroborated by improvement of molecular crystalline, mitigated Urbach energy, and increased EIS recombination resistance, which shifts the onset of photocurrent saturation to higher Φ_{opt}. In Figure 5b, the transient photo-response (TPR) characteristics of the PTB7-Th:TQC-4Cl based devices are evaluated. The pristine device exhibits a pronounced leading-edge spike, which progressively diminishes with increasing annealing temperature and eventually becomes negligible in the 200 °C annealed device. This spike can be attributed to a transient displacement current induced by the pyroelectric effect, and its systematic attenuation with increasing annealing temperature suggests a suppression of pyroelectric contributions due to enhanced film crystallinity and the elimination of locally non-centrosymmetric domains.[30] Concurrently, the carrier-transport dynamics are markedly improved. The rise time (T_r) decreases from 54.40 µs (pristine) to 53.60, 38.40, 35.20, and 16.00 µs for the 70, 110, 150, and 200 °C annealed devices, respectively, while the fall time (T_f) shortens from 23.08 µs to 22.79, 22.79, 21.80, and 20.94 µs. These results demonstrate that thermal treatment at 200 °C leads to a significant improvement in photo-response speed, supporting the conclusion that structural optimization of the bulk heterojunction is critical for achieving fast and stable operation in high-performance SWIR OPDs.

Next, device-intrinsic noise levels were obtained via noise spectral density (S_n) measurements in the dark. For accurate assessment of TQC-4Cl, ten high-resolution measurements were averaged (Figure 5c). The low noise of the devices beyond the detection capability of our equipment limited noise evaluation at higher frequencies, representing white-noise – the seemingly saturated S_n at >10 Hz represents the equipment noise floor. Therefore, RMS noise current (I_{rms}) was yielded using S_n at 4 Hz, a frequency at which all devices exhibited flicker noise. In correspondence to $I_{rms,shot}$, I_{rms} showed an increasing trend with increasing thermal annealing temperature, measured as 62.2, 122, 263, 351, and 466 fA for pristine, 70, 110, 150, and 200 °C annealed OPD devices. The lower interfacial trap densities as observed from AFM topography images and higher charge mobilities of lower-temperature-processed devices reduce random current fluctuations from charge trapping—detrapping processes, thereby reducing I_{rms} pronouncedly at flicker-dominated frequencies, as opposed to $I_{rms,shot}$. Extrapolated D^* based on S_n (D_n^*) spectra were achieved using the obtained I_{rms} values, in which the SWIR-optimum device demonstrated the highest D_n^* of 2.84×10^{11} Jones, leveraging its high R (Figure 5d).

2.6. Thermal Stability and Long-Term Reliability

Finally, we evaluated the thermal stability of the PTB7-Th:TQC-4Cl based OPD devices under continuous thermal stress. Both pristine and optimized devices were subjected to accelerated aging by maintaining them at 85 °C in N_2-filled glovebox. The D_{sh}^* and R of them were periodically measured at a wavelength of 1200 nm over the course of the test for four distinct devices, with the results presented as averages and standard deviations (**Figure 6**; Figure S28, Supporting Information). Remarkably, both devices retained D_{sh}^* values within the 10^{11}–10^{12} Jones range for over 1800 h, indicating stable noise characteristics and photo-response. Both devices also exhibited stable R throughout the aging period, further supporting their robustness under prolonged thermal stress. This outstanding thermal stability highlights the practical potential of PTB7-Th:TQC-4Cl-based devices for long-term operation in SWIR photodetection applications.

3. Conclusion

In summary, we have successfully synthesized and demonstrated a novel proquinoid-type non-fullerene acceptor, TQC-4Cl, specifically designed to overcome the intrinsic limitations of SWIR OPDs. TQC-4Cl exhibits an ultra-narrow bandgap of 1.01 eV and broad absorption extending beyond 1200 nm, enabled by a quinoid–aromatic transformation strategy that enhances π-electron delocalization across the conjugated backbone. Owing to its highly planar molecular structure and excellent thermal robustness, the TQC-4Cl film showed significantly enhanced crystallinity characterized by closed packing distances and enlarged domain sizes upon thermal annealing treatment. When employed as the photoactive material with PTB7-Th, the optimized SWIR OPDs demonstrated outstanding device performance. A remarkably suppressed J_d of 4.38×10^{-8} A cm^{-2} was achieved at –0.5 V bias, representing the lowest value reported for SWIR OPDs to date. In addition, it showed strong photo-response with an EQE of 13.66% at 1200 nm, yielding D_{sh}* surpassing 10^{12} Jones (D_n* > 10^{11} Jones) under the same bias condition. The systematic investigation of film morphology and charge transport dynamics revealed that the superior performance of PTB7-Th:TQC-4Cl-based SWIR OPDs stems from the formation of an optimized phase-separated morphology and enhanced crystallinity within the photoactive layer, which synergistically facilitates efficient charge extraction and mitigates the energetic disorder. Additionally, the thermal stability test conducted at 85 °C demonstrated that the devices maintained stable performance for over 1800 h, highlighting their potential for long-term operation under harsh conditions. This work constitutes a significant breakthrough in advancing the development of highly sensitive and thermally stable SWIR OPDs, while simultaneously expanding the molecular design landscape of ultra-narrow bandgap organic semiconductors for next-generation optoelectronic technologies.

Supporting Information

Supporting Information is available from the Wiley Online Library or from the author.

Acknowledgements

Y.C., S.J.P., and S.O. contributed equally to this work. This research was supported by the National Research Foundation of Korea (NRF) grants funded by the Korean government (RS-2024-00444458, RS-2025-00519847, and 2022R1A2C2009523) and KRICT-SKKU bilateral Research Programs.

Conflict of Interest

The authors declare no conflict of interest.

Data Availability Statement

The data that support the findings of this study are available from the corresponding author upon reasonable request

Keywords

bulk-heterojunction, non-fullerene acceptor, organic photodetector, proquinoid, short-wave infrared region

Received: July 9, 2025
Revised: August 11, 2025
Published online: October 6, 2025

---

[1] a) F. Cao, L. Liu, L. Li, *Mater. Today* **2023**, *62*, 327; b) Y. Pinki, S. Dewan, R. Mishra, S. Das, *J. Phys. D: Appl. Phys.* **2022**, *55*, 313001; c) X. Guan, X. Yu, D. Periyanagounder, M. R. Benzigar, J.-K. Huang, C.-H. Lin, J. Kim, S. Singh, L. Hu, G. Liu, D. Li, J.-H. He, F. Yan, Q. J. Wang, T. Wu, *Adv. Opt. Mater.* **2021**, *9*, 2001708; d) M. Long, P. Wang, H. Fang, W. Hu, *Adv. Funct. Mater.* **2019**, *29*, 1803807; e) M. I. Saleem, A. K. K. Kyaw, J. Hur, *Adv. Opt. Mater.* **2024**, *12*, 2401625; f) F. Yang, K. Yu, H. Cong, C. Xue, B. Cheng, N. Wang, L. Zhou, Z. Liu, Q. Wang, *ACS Photonics* **2019**, *6*, 1199.

[2] a) J. Michel, J. Liu, L. C. Kimerling, *Nat. Photonics* **2010**, *4*, 527; b) Z. Li, Z. He, C. Xi, F. Zhang, L. Huang, Y. Yu, H. H. Tan, C. Jagadish, L. Fu, *Adv. Mater. Technol.* **2023**, *8*, 2202126; c) T. Yan, L. Li, Y. Zhang, J. Hao, J. Meng, N. Shi, *Sens. Actuators, A* **2024**, *376*, 115535; d) D. Kaur, M. Kumar, *Adv. Opt. Mater.* **2021**, *9*, 2002160; e) Y. Miao, H. Lin, B. Li, T. Dong, C. He, J. Du, X. Zhao, Z. Zhou, J. Su, H. Wang, Y. Dong, B. Lu, L. Dong, H. H. Radamson, *Nanomaterials* **2023**, *13*, 606; f) A. Rogalski, *Prog. Quantum Electron.* **2003**, *27*, 59; g) Z. Lou, G. Shen, *Adv. Sci.* **2016**, *3*, 1500287; h) Y. Liu, Z. Li, F. B. Atar, H. Muthuganesan, B. Corbett, L. Wang, *ACS Appl. Mater. Interfaces* **2024**, *16*, 10996.

[3] a) J. Liu, M. Gao, J. Kim, Z. Zhou, D. S. Chung, H. Yin, L. Ye, *Mater. Today* **2021**, *51*, 475; b) J. Cong, Z.-H. Huang, S.-W. Liu, Z. Luo, Fu-Z Liu, Z. Chen, K-Mu Lee, Yu-C Huang, C. Yang, *Small* **2025**, *21*, 2410418; c) A. Wadsworth, Z. Hamid, J. Kosco, N. Gasparini, I. McCulloch, *Adv. Mater.* **2020**, *32*, 2001763; d) S. Park, K. Fukuda, M. Wang, C. Lee, T. Yokota, H. Jin, H. Jinno, H. Kimura, P. Zalar, N. Matsuhisa, S. Umezu, G. C. Bazan, T. Someya, *Adv. Mater.* **2018**, *30*, 1802359; e) S. Cai, X. Xu, W. Yang, J. Chen, X. Fang, *Adv. Mater.* **2019**, *31*, 1808138; f) G. Simone, M. J. Dyson, S. C. J. Meskers, R. A. J. Janssen, G. H. Gelinck, *Adv. Funct. Mater.* **2020**, *30*, 1904205.

[4] a) J. Miao, F. Zhang, *Laser Photonics Rev.* **2019**, *13*, 1800204; b) Z. Zhao, C. Xu, L. Niu, X. Zhang, F. Zhang, *Laser Photonics Rev.* **2020**, *14*, 2000262; c) L. Shi, Q. Liang, W. Wang, Y. Zhang, G. Li, T. Ji, Y. Hao, Y. Cui, *Nanomaterials* **2018**, *8*, 713; d) J. Chen, C. Q. Y. Huang, X. Zhang, S. Dong, X. Yang, *IEEE J. Electron Devices Soc.* **2025**, *13*, 73; e) X. Chen, A. Shi, K. Bai, W. Chen, Y. Long, Y. Li, F. Lu, *Org. Electron.* **2025**, *144*, 107276.

[5] a) J. H. Kim, A. Liess, M. Stolte, A.-M. Krause, V. Stepanenko, C. Zhong, D. Bialas, F. Spano, F. Würthner, *Adv. Mater.* **2021**, *33*, 2100582; b) N. Li, Z. Lan, Y. S. Lau, J. Xie, D. Zhao, F. Zhu, *Adv. Sci.* **2020**, *7*, 2000444; c) N. Li, P. Mahalingavelar, J. H. Vella, D.-S. Leem, J. D. Azoulay, T. N. Ng, *Mater. Sci. Eng.: R: Rep.* **2021**, *146*, 100643; d) Z. Wu, Y. Zhai, H. Kim, J. D. Azoulay, T. N. Ng, *Acc. Chem. Res.* **2018**, *51*, 3144; e) X. Gong, M. Tong, Y. Xia, W. Cai, J. S. Moon, Y. Cao, G. Yu, C.-L. Shieh, B. Nilsson, A. J. Heeger, *Science* **2009**, *325*, 1665.

[6] a) C. Yan, S. Barlow, Z. Wang, He Yan, A. K.-Y. Jen, S. R. Marder, X. Zhan, *Nat. Rev. Mater.* **2018**, *3*, 18003; b) J. Hou, O. Inganäs, R. H. Friend, F. Gao, *Nat. Mater.* **2018**, *17*, 119; c) Y. Zhang, Y. Yu, X. Liu, J. Miao, Y. Han, J. Liu, L. Wang, *Adv. Mater.* **2023**, *35*, 2211714; d) J. Yuan, Y. Zhang, L. Zhou, G. Zhang, H.-L. Yip, T.-K. Lau, X. Lu, C. Zhu, H. Peng, P. A. Johnson, M. Leclerc, Y. Cao, J. Ulanski, Y. Li, Y. Zou, *Joule* **2019**, *3*, 1140; e) Y. Wang, J. Wang, J. Miao, J. Liu, L. Wang, *CCS Chemistry* **2024**, *6*, 2794.

[7] a) J. Lee, S.-J. Ko, M. Seifrid, H. Lee, B. R. Luginbuhl, A. Karki, M. Ford, K. Rosenthal, K. Cho, T.-Q. Nguyen, G. C. Bazan, *Adv. Energy Mater.***2018**, *8*, 1801212; b) J. Huang, J. Lee, J. Vollbrecht, V. V. Brus, A. L. Dixon, D X. Cao, Z. Zhu, Z. Du, H. Wang, K. Cho, G. C. Bazan, T.-Q. Nguyen, *Adv. Mater.* **2020**, *32*, 1906027; c) J.-W. Ha, A. Y Lee, H. Ju Eun, J.-H. Kim, H. Ahn, S. Park, C. Lee, D. W. Seo, J. Heo, S. C. Yoon, S.-J. Ko, J. H. Kim, *ACS Nano* **2023**, *17*, 18792; d) W. Zhong, X. Wang, W. Wang, Z. Song, Y. Tang, B. Chen, T. Yang, Y. Liang, *Adv. Sci.* **2025**, *12*, 2410332; e) U.-H. Lee, B. Park, S. Rhee, J.-W. Ha, D. R. Whang, H. J. Eun, J. H. Kim, Y. Shim, J. Heo, C. Lee, B. J. Kim, S. C. Yoon, J. Lee, S.-J. Ko, *Adv. Opt. Mater.* **2023**, *11*, 2300312.

[8] a) Y. Wei, H. Chen, T. Liu, S. Wang, Y. Jiang, Yu Song, J. Zhang, X. Zhang, G. Lu, F. Huang, Z. Wei, H. Huang, *Adv. Funct. Mater.* **2021**, *31*, 2106326; b) Y. Xia, C. Geng, X. Bi, M. Li, Y. Zhu, Z. Yao, X. Wan, G. Li, Y. Chen, *Adv. Opt. Mater.* **2024**, *12*, 2301518.

[9] a) M. Yang, B. Yin, G. Hu, Y. Cao, S. Lu, Y. Chen, Y. He, X. Yang, B. Huang, J. Li, B. Wu, S. Pang, L. Shen, Y. Liang, H. Wu, L. Lan, G. Yu,

F. Huang, Y. Cao, C. Duan, *Chem* **2024**, *10*, 1425; b) T. Li, G. Hu, L. Tao, J. Jiang, J. Xin, Y. Li, W. Ma, L. Shen, Y. Fang, Y. Lin, *Sci. Adv.*, *9*, adf6152; c) Y. Chen, Y. Zheng, J. Wang, X. Zhao, G. Liu, Y. Lin, Y. Yang, L. Wang, Z. Tang, Y. Wang, Y. Fang, W. Zhang, X. Zhu, *Sci. Adv.*, *10*, adm9631; d) Y. Zhang, J. Chen, J. Yang, M. Fu, Y. Cao, M. Dong, J. Yu, S. Dong, X. Yang, L. Shao, Z. Hu, H. Cai, C. Liu, F. Huang, *Adv. Mater.* **2024**, *36*, 2406950.

[10] a) J. Huang, G. Yu, *Mater. Chem. Front.* **2021**, *5*, 76; b) Y. Kim, Y.-J. Kim, Y.-A. Kim, E. Jung, Y. Mok, K. Kim, H. Hwang, J.-J. Park, M.-G. Kim, S. Mathur, D.-Y. Kim, *ACS Appl. Mater. Interfaces* **2021**, *13*, 2887.

[11] K. Kawabata, M. Saito, I. Osaka, K. Takimiya, *J. Am. Chem. Soc.* **2016**, *138*, 7725.

[12] a) K. Kawabata, K. Takimiya, *Chem.-Eur. J.* **2021**, *27*, 15660; b) T. Mikie, I. Osaka, *J. Mater. Chem. C* **2020**, *8*, 14262.

[13] a) S. Steinberger, A. Mishra, E. Reinold, E. Mena-Osteritz, H. Müller, C. Uhrich, M. Pfeiffer, P. Bäuerle, *J. Mater. Chem.* **2012**, *22*, 2701; b) Y. Bai, J. Rawson, S A. Roget, J.-H. Olivier, J. Lin, P. Zhang, D. N. Beratan, M. J. Therien, *Chem. Sci.* **2017**, *8*, 5889; c) K. Susumu, T. V. Duncan, M. J. Therien, *J. Am. Chem. Soc.* **2005**, *127*, 5186; d) W. Cao, X. Zhang, X. Yang, H. Sun, Z. Chen, Y. Liang, *ACS Mater. Lett.* **2024**, *6*, 2687.

[14] a) M. Karikomi, C. Kitamura, S. Tanaka, Y. Yamashita, *J. Am. Chem. Soc.* **1995**, *117*, 6791; b) J. Casado, R. P. Ortiz, M. C. Ruiz Delgado, V. Hernández, J. T. López Navarrete, J.-M. Raimundo, P. Blanchard, M. Allain, J. Roncali, *J. Phys. Chem. B* **2005**, *109*, 16616; c) J. Roncali, *Macromol. Rapid Commun.* **2007**, *28*, 1761.

[15] a) T. L. D. Tam, C. K. Ng, S. L. Lim, E. Yildirim, J. Ko, W. L. Leong, S.-W. Yang, J. Xu, *Chem. Mater.* **2019**, *31*, 8543; b) T. L. D. Tam, G. Wu, S. W. Chien, S. F. V. Lim, S.-W. Yang, J. Xu, *ACS Mater. Lett.* **2020**, *2*, 147; c) T. L. Dexter Tam, A. Moudgil, W. J. Teh, Z. M. Wong, A. D. Handoko, S. W. Chien, S.-W. Yang, B. S. Yeo, W. L. Leong, J. Xu, *J. Phys. Chem. B* **2022**, *126*, 2073.

[16] R. Lv, S. Geng, S. Li, F. Wu, Y. Li, T. R. Andersen, Y. Li, X. Lu, M. Shi, H. Chen, *Sol. RRL* **2020**, *4*, 2000286.

[17] H. Zhang, R. Mao, L. Yuan, Y. Wang, W. Liu, J. Wang, H. Tai, Y. Jiang, *ACS Appl. Mater. Interfaces* **2024**, *16*, 9088.

[18] B. Yin, X. Zhou, Y. Li, G. Hu, W. Wei, M. Yang, S. Jeong, W. Deng, B. Wu, Y. Cao, B. Huang, L. Pan, X. Yang, Z. Fu, Y. Fang, L. Shen, C. Yang, H. Wu, L. Lan, F. Huang, Y. Cao, C. Duan, *Adv. Mater.* **2024**, *36*, 2310811.

[19] Y. Wang, M. Yang, B. Yin, B. Wu, G. Liu, S. Jeong, Y. Zhang, C. Yang, Z. He, F. Huang, Y. Cao, C. Duan, *ACS Appl. Mater. Interfaces* **2024**, *16*, 66846.

[20] a) L. Wang, H. Wang, S. Yu, N. An, Y. Pan, J. Li, T. Jia, K. Wang, W. Huang, *Adv. Funct. Mater.* **2024**, *34*, 2315762; b) Y. Joo, L. Huang, N. Eedugurala, A. E. London, A. Kumar, B. M. Wong, B. W. Boudouris, J. D. Azoulay, *Macromolecules* **2018**, *51*, 3886.

[21] a) W. Liu, S. Deng, L. Zhang, C.-W. Ju, Y. Xie, W. Deng, J. Chen, H. Wu, Y. Cao, *Adv. Mater.* **2023**, *35*, 2302924; b) M. Liang, L. Liu, Y. Sun, J. Li, L. Zhang, X. Jiang, W. Wu, *Aggregate* **2024**, *5*, 458.

[22] F. Verstraeten, S. Gielen, P. Verstappen, J. Raymakers, H. Penxten, L. Lutsen, K. Vandewal, W. Maes, *J. Mater. Chem. C* **2020**, *8*, 10098.

[23] I. Park, C. Kim, R. Kim, N. Li, J. Lee, O. K. Kwon, B. Choi, T. N. Ng, D.-S. Leem, *Adv. Opt. Mater.* **2022**, *10*, 2200747.

[24] H. M. Luong, S. Chae, A. Yi, K. Ding, J. Huang, B. M. Kim, C. Welton, J. Chen, H. Wakidi, Z. Du, H. J. Kim, H. Ade, G. N. M Reddy, T.-Q. Nguyen, *ACS Energy Lett.* **2023**, *8*, 2130.

[25] a) W. Jang, S. Rasool, B. G. Kim, J. Kim, J. Yoon, S. Manzhos, H. K. Lee, I. Jeon, D. H. Wang, *Adv. Funct. Mater.* **2020**, *30*, 2001402; b) X. Huang, Z. Zhao, S. Chung, K. Cho, J. Lv, S. Lu, Z. Kan, *J. Mater. Chem. C* **2022**, *10*, 17502.

[26] A. Özmen, Y. Yakar, B. Çakır, Ü. Atav, *Opt. Commun.* **2009**, *282*, 3999.

[27] V. D. Mihailetchi, H. X. Xie, B. de Boer, L. J. A. Koster, P. W. M. Blom, *Adv. Funct. Mater.* **2006**, *16*, 699.

[28] H. Quan, Z. Zhong, T. Hao, K. An, W. Zhong, C. Wang, F. Liu, L. Ying, F. Huang, *Chem. Eng. J.* **2023**, *452*, 139295.

[29] N. Zarrabi, O. J. Sandberg, S. Zeiske, W. Li, D. B. Riley, P. Meredith, A. Armin, *Nat. Commun.* **2020**, *11*, 5567.

[30] a) Y. Huang, L. Shao, Y. Wang, L. Hao, X. Luo, J. Zheng, Y. Cao, S. Li, Z. Tan, S. Li, W. Zhong, S. Dong, X. Yang, J. Benduhn, C. Liu, K. Leo, F. Huang, *Adv. Mater.* **2025**, *37*, 2500491; b) Q. Li, Z. Li, J. Meng, *Int. J. Optomechatr.* **2022**, *16*, 1.